



# Realization of multilocal gradient-doping PCN by alkali metal ion sustained release capsules for enhanced photocatalytic water splitting

Jiawei Yan<sup>a</sup>, Wenjian Fang<sup>a,c,\*</sup>, Zhidong Wei<sup>a,b</sup>, Jiasheng Chi<sup>a</sup>, Mingxia Chen<sup>a</sup>, Zhi Jiang<sup>a</sup>, Kun Jiang<sup>d</sup>, Shaohua Shen<sup>e</sup>, Wenfeng Shangguan<sup>a,\*\*</sup>

<sup>a</sup> Research Center for Combustion and Environment Technology, Shanghai Jiao Tong University, Shanghai 200240, China

<sup>b</sup> College of Smart Energy, Shanghai Jiao Tong University, Shanghai 200240, China

<sup>c</sup> School of Electrical and Energy Power Engineering, Yangzhou University, Yangzhou 225002, China

<sup>d</sup> Institute of Fuel Cells, Shanghai Jiao Tong University, Shanghai 200240, China

<sup>e</sup> International Research Center for Renewable Energy, State Key Laboratory of Multiphase Flow in Power Engineering, Xi'an Jiaotong University, Xi'an 710049, China

## ARTICLE INFO

### Keywords:

Doping  
Photocatalysis  
Ion diffusion  
Potential well  
Charge transfer

## ABSTRACT

The gradient-doping technique has been widely applied to induce an oriented built-in electric-field. However, it is still not efficient enough for charge mobility especially for particulate semiconductors, as the field is primarily in one direction from inner to surface. Here, we propose a multilocal gradient-doping technique that a nano-capsule is designed to store dopants and then release them into semiconductors nonuniformly. As an illustration, scattered pyrochlore-type  $\text{K}_2\text{Ta}_2\text{O}_6$  nanoparticles have been validated the capability of storing and releasing  $\text{K}^+$ , which subsequently diffuse into the substrate PCN. Multi point-radiative gradient in  $\text{K}^+$  concentration, confined within the  $\text{K}_2\text{Ta}_2\text{O}_6$ 's vicinity, will construct several 3D potential wells which can not only accelerate the carrier separation but also offer more migration channels for both photo-induced electrons and holes to the surface. Consequently, the multilocal  $\text{K}^+$  gradient-doping PCN shows the longest carriers' lifetime and highest AQY ( $\sim 21.8\%$  at 400 nm) compared with the other uniformly doping techniques.

## 1. Introduction

The direct conversion of solar energy into electrical energy or chemical energy by semiconductor materials is a promising path to resource sustainability and carbon neutrality [1,2], but it encounters the insufficient separation of photo-induced electrons and holes regarded as one dominant inhibition for attaining satisfactory energy conversion efficiencies [3–5]. The creation and enhancement of a built-in electric-field, which is tightly associated with internal symmetry breaking and band structure engineering, have been widely used to improve the charge separation of semiconductor materials [5–7]. Various strategies have been proposed to induce a built-in electric-field, including junction construction [8], morphological selective-facets control [9,10], and asymmetric co-catalyst assembling [9,11]. Among them, the rational-designed gradient doping strategy is considered effective to construct a built-in electric-field oriented along the concentration gradient by building a consecutive band bending structure [12,13] has been thoroughly investigated in many fields, including photocatalysis

[14–16], photovoltaics [17,18], and photoelectrochemical [19–23] water splitting. For example, Xiao et al. recently reported a photoanode based on the gradient Mg-doped  $\text{Ta}_3\text{N}_5$  which can deliver a low onset potential (0.4 V vs. RHE) and a high applied bias photon-to-current efficiency of  $3.25 \pm 0.05\%$  [24]. The enhanced asymmetric electric-field induced by gradient doping facilitates the extraction and migration of photo-induced carriers, consequently leading to much superior separation efficiency compared with typical uniform doping.

Despite a few studies about the realization of gradient-doping in particulate semiconductors, the built-in electric-field in these semiconductor materials is primarily confined in the near-surface region in one direction from inner to surface. It is not efficient enough for charge mobility that the charges may also migrate and recombine in the other two directions. Particularly, surface catalytic reactions occur at random points in nanoconfined catalysis. The oriented built-in electric-field cannot prevent the charge recombination in the surface layer. Furthermore, the gradient-doping in particulate semiconductors provides only a single channel for photo-induced electrons (or holes) transporting to the

\* Corresponding author at: Research Center for Combustion and Environment Technology, Shanghai Jiao Tong University, Shanghai 200240, China.

\*\* Corresponding author.

E-mail addresses: [fwjlf2227@163.com](mailto:fwjlf2227@163.com) (W. Fang), [shangguan@sjtu.edu.cn](mailto:shangguan@sjtu.edu.cn) (W. Shangguan).

<https://doi.org/10.1016/j.apcatb.2023.123155>

Received 16 June 2023; Received in revised form 28 July 2023; Accepted 4 August 2023

Available online 6 August 2023

0926-3373/© 2023 Elsevier B.V. All rights reserved.

surface, and meanwhile retained photo-induced holes (or electrons) would stay in the inner. Thus, decorating particulate semiconductors with multilocal gradient-doping distribution is significant and challenging that the doping ions should be injected into the nanoparticles both continuously in time and nonuniformly in space. Traditional methods for gradient-doping, such as electron-beam evaporation and magnetron sputtering, fail to inject the doping ions onto the surface nonuniformly. Especially for particulate semiconductors, the doping ions are generally mixed with materials thoroughly, which is also difficult to realize nonuniformly in space.

Inspired by the ‘sustained-release tablets’, we design a nano-capsule to store the dopants which can be released during the nanomaterial synthesis. Herein, we demonstrate and exploit the ion storing and releasing capability of the defective pyrochlore structure to realize the localized gradient doping distribution via ion point-diffusion. Pyrochlore structure ( $A_2B_2O_6$ ) displays a rigid corner-shared  $BO_6$  octahedral network with channels, which is suitable for storage and motion of cations A [25,26]. The defective pyrochlore-type  $K_2Ta_2O_6$  ( $KTO_{pyr}$ ) is hence chosen as the doping source of  $K^+$ . Besides, graphitic polymeric carbon nitride (PCN) as one representative two-dimensional material always shows the high recombination of charge carriers [27–32]. Various effective doping modifications have been reported to enhance the photo-induced carrier separation including alkali-metal ions (e.g.,  $Na^+$ ,  $K^+$ ) doping, while the carrier separation efficiency is still restrained by the disordered ion distribution resulting from the uniformly doping process [33–37]. Therefore, we will take  $KTO_{pyr}$  particles as the diffusible  $K^+$  source and PCN as the substrate, to realize the multilocal gradient-doping. Here, multilocal gradient  $K^+$  doped PCN sample, abbreviated as (K)PCN&KTO, is designed via embedding  $KTO_{pyr}$  particles into PCN layers.

## 2. Experimental procedures

### 2.1. Preparation of materials

- (a) Synthesis of defective pyrochlore  $K_2Ta_2O_6$ : 0.02 mol tantalum oxide (99.99% metal basis, Macklin) were added into 100 mL 8.5 M KOH solution (GR, Sinopharm Chemical Reagent) with vigorous stirring for 4 h. Then the obtained white suspension was transferred into a Teflon-lined stainless-steel autoclave (200 mL) followed by the hydrothermal process at 160 °C for 8 h. The resultant white precipitates were centrifuged with deionized water to sufficiently remove excessive KOH and then dried at 80 °C in vacuum overnight [38,39]. The pyrochlore-type  $K_2Ta_2O_6$  particles were ultimately obtained following by the calcination at 600 °C in air for the better crystallization. For convenience,  $KTO_{pyr}$  was representative of defective pyrochlore-type  $K_2Ta_2O_6$  unless otherwise specified.
- (b) Synthesis of perovskite  $KTaO_3$ : The synthetic procedures were the same as that of  $KTO_{pyr}$  except that the concentration of KOH solution was 15 M and the hydrothermal temperature was 200 °C. For convenience,  $KTO_{per}$  was representative of perovskite-type  $KTaO_3$  unless otherwise specified.
- (c) Synthesis of (K)PCN&KTO-x sequence: The as-obtained  $KTO_{pyr}$  particles and 20 g urea (AR, General-reagent) were ground thoroughly in a mass ratio x ranging from 0.5% to 10%. The mixture was transferred into a crucible (50 mL) which was fully sealed by tin foils and then calcinated at 550 °C in a muffle furnace for 4 h with a heating rate of 2.3 °C /min. After the annealing, the collected products were purified with deionized water and dried at 80 °C in vacuum overnight. It was worth noting that, (K)PCN&KTO was representative of (K)PCN&KTO-x ( $x = 3.75\%$ ) sample for convenience unless otherwise specified.
- (d) Synthesis of (K)PCN& $KTO_{per}$  sample: The synthetic procedures were the same as that of (K)PCN&KTO except for the substitution of  $KTO_{per}$  particles for  $KTO_{pyr}$  particles.

- (e) Synthesis of (K)PCN&KOH sample: 20 g urea was dispersed into an aqueous KOH solution containing appropriate amounts of KOH (the same  $K^+$  addition to that of (K)PCN& $KTO$ -x sequence) by ultrasonication and the mixture was evaporated in a water bath at 80 °C with vigorous stirring. The dry powders were fully ground and the following annealing procedures were the same as that of (K)PCN&KTO sequence.
- (f) Synthesis of (K)PCN& $KTO(I)$ : The synthetic procedures were the same as that of (K)PCN& $KTO$ -x sequence except for the substitution of the grind process for the impregnation process.
- (g) Synthesis of (K)PCN& $KTO(M)$ : The as-obtained  $KTO_{pyr}$  particles and urea were ground in mechanical mixing without the subsequent polymerization.
- (h) Synthesis of pristine PCN sample: The synthetic procedures were the same as that of (K)PCN&KTO sequence except for the absence of  $KTO_{pyr}$  particles.
- (i) Synthesis of T-t sample: The as-obtained  $KTO_{pyr}$  particles and PCN are treated by secondary annealing at temperature (T) for time (t) in the same sealing method as (c).
- (j)  $K^+$ - $Na^+$  ion exchange: The as-obtained  $KTO_{pyr}$  particles were dispersed into 6 M NaOH solution in a water bath (80 °C) with thorough blending for 12 h. After the centrifugation for the removal of excessive NaOH,  $Na_2Ta_2O_6$  with pyrochlore structure (abbreviated as NTO) was derived via the A-site ion substitution. Similarly, NTO can be transformed to  $KTO_{pyr}$  again after being fully stirred in 6 M KOH solution.
- (k) Synthesis of  $Na^+$  doping sample: (Na)PCN&NaOH and (Na)PCN&NTO samples were produced in the same way with the substitution of K-containing precursors for Na-containing precursors.
- (l) Synthesis of (K)PCN&KOH× $KTO$ : The as-obtained  $KTO_{pyr}$  particles and as-obtained (K)PCN&KOH sample were combined in the same ratio following the impregnation process.
- (m) Synthesis of (K)PCN&KCl and (K)PCN& $KNO_3$ : The synthetic procedures were the same as that of (K)PCN&KOH except for the substitution of KOH for KCl and  $KNO_3$  in the same ratio, respectively.
- (n) Synthesis of (K)PCN-KTO (two-step): The as-obtained  $KTO_{pyr}$  particles and as-obtained PCN sample were ground and then treated with the same calcination condition to (K)PCN&KTO sample.

### 2.2. Structural characterizations

Powder X-ray diffraction (XRD) patterns were measured on an X-ray diffractometer (Mini Flex 600, Rigaku, Tokyo, Japan) using Cu-K $\alpha$  as the X-ray source at 40 kV voltage and 15 mA current. The diffraction angle (2 $\theta$ ) range was from 5° to 90° with a scan speed of 15°/min. In-situ temperature-programed XRD patterns were measured at a scan speed of 2°/min on an X-ray diffractometer (D8 Advance, Bruker, Karlsruhe, Germany) using Co as the X-ray source at 35 kV voltage and 40 mA current. The conversion of XRD patterns with Co ( $\lambda = 1.78 \text{ \AA}$ ) and Cu ( $\lambda = 1.54 \text{ \AA}$ ) was realized by Bragg equation. The resultant diffraction patterns and corresponding crystal structures were further analyzed by Jade 6.5 software. The light absorption property was reflected by powder ultraviolet-visible (UV-vis) diffuse reflection spectra (DRS) on a UV-vis spectrophotometer (UV-2450, Shimadzu, Kyoto, Japan) fitted by an integrating sphere assembly with pure  $BaSO_4$  as the reference. The chemical structures and functional groups of samples were identified from Fourier transform infrared spectroscopy (FT-IR) collected by a FT-IR spectrometer (Nicolet 6700, Thermo Fisher Scientific, Massachusetts, USA) equipped with an integrating sphere for mid-infrared region over the range 4000  $cm^{-1}$  - 400  $cm^{-1}$  with a resolution of 2  $cm^{-1}$ . Solid-state  $^{13}C$  cross polarization magic angle spinning total suppression of sidebands (CP-MAS-TOSS) nuclear magnetic resonance (NMR) spectra were recorded by a solid-state NMR spectrometer (Avance neo 600 MHz,

Bruker, Karlsruhe, Germany) to determine the conversion of functional groups. An electron paramagnetic resonance (EPR) spectrometer (EMX-8, Bruker, Karlsruhe, Germany) was applied to collect EPR spectroscopy at room-temperature. X-ray photoelectron spectroscopy (XPS) measurements were carried out on a XPS spectrometer (AXIS UltraDLD, Kratos, Manchester, British) using a monochromatic Mg-K $\alpha$  radiation, in which binding energies were calibrated by C 1s peak at 284.6 eV to determine the chemical composition and electronic state of samples. The microstructure and morphology of samples were observed via a field-emission scanning electron microscopy (SEM) (RISE-MAGNA, Tescan, Brno, Czech Republic and Sirion 200, FEI, Oregon, America). A field-emission transmission electron microscopy (FE-TEM) with element mapping (TALOS F200X G2, FEI, Oregon, America) was applied to acquire high-resolution TEM images and the relative element contents of samples. Raman spectra in spatial resolution were performed on a correlative Raman imaging and scanning electron microscopy (RISE) (Magna, Tescan, Brno, Czech Republic) cooperated with a laser confocal Raman Microspectroscopy (Apyron, WITec, Ulm, Germany). The room-temperature steady-state photoluminescence (PL) emission spectra and time-resolved transient PL decay spectra measurements were conducted on a PL spectrometer (FLS1000, Edinburgh Instruments, Edinburgh, British) under the excitation of a 390 nm continuous laser.

### 2.3. Photoelectrochemical measurements

All electrochemical measurements were carried out on an electrochemical workstation (PARSTAT 4000, Princeton Applied Research, California, USA) in three-electrode configuration. A Pt coil and an Ag/AgCl (3.5 M KCl) electrode were used as the counter electrode and reference electrode, respectively. A solar simulator was applied as the light source and its intensity was calibrated to 100 mW cm<sup>-2</sup>. The working electrode was prepared by the spin-coating method conducted on a spin coater (EZ4-S-PP, Schwan technology, Minnesota, USA). The coated ink was composed of 50 mg sample and 0.5 mL tailor-made binder solution (a sticky transparent dissolved ethyl cellulose solution (0.5 g) with absolute ethyl alcohol (15 mL) and turpentine (23.3 g) as solvents) with thorough mixing and then was evenly pasted onto the conductive-side of a (1.5 cm  $\times$  1.5 cm) fluorine-doped tin oxide (FTO) substrate followed by the spin-coating procedure [40]. Then the resultant uniform-coated FTO substrate was annealed at 300 °C for 2 h with a heating rate of 3 °C/min and cooled down naturally as working electrodes for the following electrochemical measurements.

The photocurrent density measurement was implemented in a three-electrode cell containing 0.1 M Na<sub>2</sub>SO<sub>4</sub> solution (PH = 6.8) applied with a bias voltage of 0.6 V (vs. Ag/AgCl) under intermittent light irradiation controlled by a shutter through a (1 cm  $\times$  1 cm) window. The electrochemical and photoelectrochemical impedance spectroscopy (EIS and PEIS) was acquired in the frequency variation ranging from 0.1 to 10<sup>5</sup> Hz at an open-circuit potential with an amplitude of 5 mV under darkness and illumination condition. Mott-Schottky (M-S) plots were measured at 500 and 1000 Hz stimulated by the sinusoidal wave with an amplitude of 5 mV under darkness condition.

### 2.4. Hydrogen evolution measurements

Photocatalytic hydrogen evolution performances were evaluated in a Pyrex reaction cell (200 mL) connected to a gas circulation system and an evacuation system. Briefly, 50 mg sample was dispersed in a methyl alcohol aqueous solution (100 mL containing 20 vol% methyl alcohol) with an ultrasonication for 10 min. Then an appropriate content (340  $\mu$ L) of H<sub>2</sub>PtCl<sub>6</sub> with a concentration of 1.48 mg(Pt)/mL was added, which corresponded to 1 wt% Pt loading on photocatalysts. Applying a 300 W xenon lamp (CEL-HXF 300, Beijing China Education Au-light Co., Ltd., Beijing, China) at a 300–800 nm wavelength range as the light source equipped with a cold mirror and an ultraviolet cut-off (> 420 nm) filter, the in-situ photodeposition of Pt was achieved through successive

evacuation and top-irradiation for 2 h. The hydrogen generation tests were commenced after the reaction cell was vacuumed again followed by the in-situ photodeposition. The generated hydrogen was detected on gas chromatography (GC-9860, Qiyang, Shanghai, China) equipped with a thermal conductivity detector using pure argon as the gas carrier. The mass concentration curve for photocatalysts was collected in the same condition except for the mass variation.

The measurement of the apparent quantum yield (AQY) of hydrogen evolution from water formed on (K)PCN&KTO-3.75% sample was implemented on a 300 W xenon lamp with given bandpass filters at 365, 380, 400, 420 and 450 nm, and the corresponding average incident light intensity was recorded by an optical densitometer (CEL-NP2000, Beijing China Education Au-light Co., Ltd., Beijing, China). The irradiation area of the reactor was 19.6 cm<sup>2</sup> and the mass concentration of samples was still 50 mg in 100 mL solution (containing 10 vol% TEOA). The AQY was calculated according to the following formula:

$$\text{AQY} = \frac{2 \times \bar{n}_{\text{H}_2}}{\text{Number of incident photons}} \times 100\%$$

### 2.5. Computational methods

All periodic band structures and density of states (DOS) calculations were performed on the CASTEP software based on density functional theory (DFT). The exchange-correlation effects were taken into consideration using the Perdew-Burke-Ernzerhof (PBE) within the spin-polarized generalized gradient approximation (GGA) [41,42]. In the computational procedure, a cutoff energy of 570 eV and a Monkhorst–Pack grid of 3  $\times$  3  $\times$  1 were used. Geometry optimizations were done before single-point energy calculation. The convergence tolerance for self-consistent convergence was set at 5  $\times$  10<sup>-6</sup> eV/atom; the convergence tolerance for the maximal force was set at 0.01 eV/Å; the convergence tolerance for the stress was set at 0.02 GPa. Structure models PCN-O<sub>x</sub> (x = 2, 4) represent pure CN configuration with half of the rings open and all rings open, respectively. (K<sub>y</sub>)PCN-O<sub>x</sub> (y = 1, 2) represent K<sup>+</sup> embedding CN configuration with the atomic ratio K/N of 1/36 and 1/18, respectively.

## 3. Results and discussion

Multilocal gradient K<sup>+</sup> doped PCN sample, abbreviated as (K)PCN&KTO, is designed via embedding KTO<sub>pyr</sub> particles into PCN layers. Schematically shown in Fig. 1a, b is the point-diffusion-controlled K<sup>+</sup> ion release triggered by K<sup>+</sup> extraction inside the doping source (KTO<sub>pyr</sub> particles) and subsequently ion-diffusion in the substrate (PCN layers) with the consequent K<sup>+</sup> gradient distribution confined in the particle's vicinity. The corresponding consecutive bending in conduction band is hence constructed along with the gradient in K<sup>+</sup> concentration. The resulting point-source radiate K<sup>+</sup> distribution within each particle's vicinity creates a built-in electric-field that is similar to the point-charge system. Consequently, the nanoscale superimposed built-in electric-field is then established between particles and leads to the localized uneven CBM (conduction band minimum) potential surface with ups and downs, as schematically shown in Fig. 1e. Driven by this 3D potential well, photo-excited charge carriers are inclined to separate in opposite directions as electrons are facilitated to migrate and accumulate at the peak in the relative positive potential level, thus reducing the probability of recombination and promoting the efficiency of transfer. Remarkably, multilocal potential wells can also offer more migration channels for both photo-induced electrons and holes to the surface.

KTO<sub>pyr</sub> octahedral particles (Figure 1di) in clusters wrapped tightly by PCN layers are vividly shown in Figure 1dii and Figure 2aiv. A controlled radiate K<sup>+</sup> point-diffusion is introduced due to the steady ion-release capacity of KTO<sub>pyr</sub> particles. The theoretical atomic arrangement for pyrochlore structure (KTO<sub>pyr</sub>) is displayed in Figure 1ci, cii. KTO<sub>pyr</sub> is constructed with corner-shared TaO<sub>6</sub> octahedral units arrayed in a



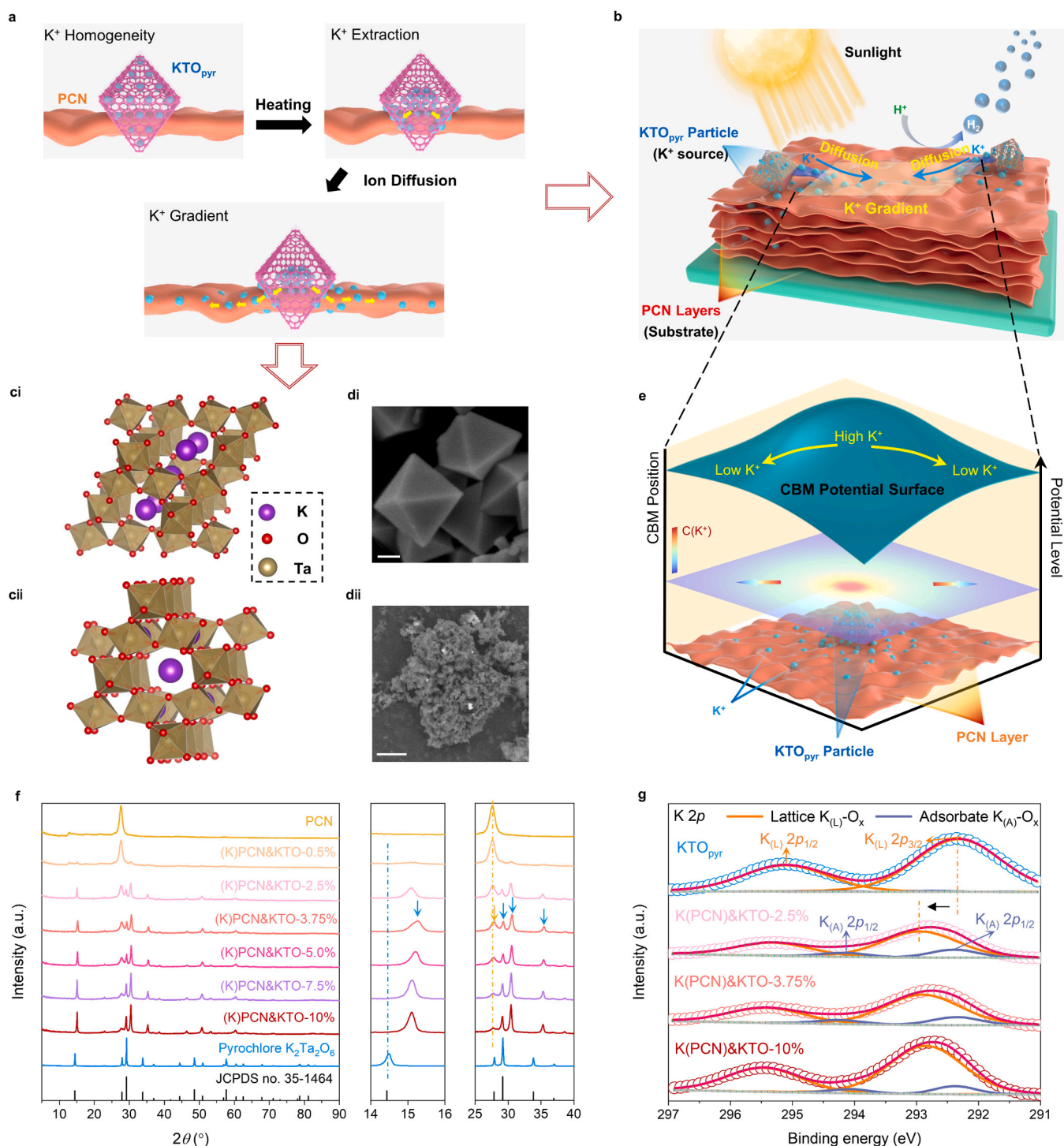


**Fig. 1.** a-b, e, Schematic illustrations of K<sup>+</sup> ion release controlled via point-diffusion occurring on PCN substrate with the resulting gradient K<sup>+</sup> doping distribution, which exhibits an outstanding photocatalytic performance in hydrogen evolution. ci-cii, The atomic arrangement of KTO<sub>pyr</sub> crystalline structure, which displays a unique coadjacent network with 3D-channels for K<sup>+</sup> storing and transfer. di-dii, The morphology characterization and microstructure observed in SEM imaging. The scale bars are 200 nm in di and 2 μm in dii, respectively. Octahedral KTO<sub>pyr</sub> particles (di) are embedded into the substrate and tightly wrapped by PCN layers (dii). f, X-ray diffraction patterns. The zoomed-in images on the right side show characteristic peaks for KTO<sub>pyr</sub> (blue arrow) and PCN (yellow arrow) respectively in the low-angle region. g, XPS core-level spectra of K 2p after peak-differentiating and imitating. Two doublets correspond to surface K-O<sub>x</sub> associated with the oxygen from KTO<sub>pyr</sub> lattice (K<sub>(L)</sub>) and from adsorbates (K<sub>(A)</sub>), respectively. The matching between the sample sequence and line colors is normalized to all figures in this manuscript.

The potential contour of CBM level with ups and downs is introduced by the point-source radiate K<sup>+</sup> doping distribution (e), which facilitates to the directional migration of photo-induced electrons and inhibition of charge recombination. Spectral measurements (f-g) are the comparison of pristine PCN and (K)PCN&KTO-x sequence to investigate the relationship between the doping source addition and the doping effects.



zigzag-like configuration along the [100] direction and each corner in the unit is surrounded with a hexagonal cavity in which a  $\text{KO}_4$  tetrahedron is embedded [26,43]. The unique coadjacent network contributes to the formation of 3D-connected channels storable for  $\text{K}^+$  (colored in purple) and available for ion motion. The ion release is further verified by the distinct peak shift in diffraction patterns and the significant decline in the atomic ratio of K/Ta as a flow of  $\text{K}^+$  drains away from  $\text{KTO}_{\text{pyr}}$  particles. The K/Ta in (K)PCN&KTO sample is determined to be 0.24 (Fig. S2 and Table S1), which decreases to nearly half compared to pristine  $\text{KTO}_{\text{pyr}}$  (0.41–0.44). It should be noted that the non-stoichiometric deficiency with the deviation of K/Ta from the formula value in both (K)PCN&KTO sample and pristine  $\text{KTO}_{\text{pyr}}$  do not change the intrinsic structure and capacity. Because the pyrochlore structure could tolerate vacancies at A-site cation with good structural stabilization [26], the fundamental crystalline structure of  $\text{KTO}_{\text{pyr}}$  is still maintained in spite of the massive  $\text{K}^+$  outflow, supported by the characteristic diffraction pattern of pyrochlore-type (Fig. 1f and Fig. S1). Furthermore, the discharging and the volatilization of  $\text{K}^+$  are not found (Fig. S1c) with  $\text{KTO}_{\text{pyr}}$  being heated separately, which implies the thermal stability at a lower temperature ( $< 600^\circ\text{C}$ ). In contrast, a progressive increasing shift towards a larger angle for all diffraction peaks representative of  $\text{KTO}_{\text{pyr}}$  (Fig. S1b, d) with the increasing time and temperature indicates the irreversible lattice contraction caused by the  $\text{K}^+$  discharging, which sustains the fact that ion release indeed occurs. The impetus of the controlled  $\text{K}^+$  release is derived from the intensified chemical inhomogeneity caused by the segregation of  $\text{K}^+$  on heating in the near-surface region of  $\text{KTO}_{\text{pyr}}$  particles, which is supported by the significant upward shift towards higher BE of  $\text{K}_{(\text{L})}\text{-O}_x$  doublet coordinated with  $\text{Ta}^{5+}$  spectrum (Fig. S5a) and the increased intensity of  $\text{K}_{(\text{A})}\text{-O}_x$  doublet (Fig. 1g) as more surface  $\text{KO}_x$  complexes accumulate [44].

With regard to (K)PCN&KTO sample, element K is distributed in PCN obviously while no evidence is pointed to element Ta doping (Figure 2ai, aiii). The atomic ratio of K/N from inside to outside gradually drops roughly from 25% to 5% and the decline is fitted well for the logarithmic trend as shown in Fig. 2d, which indicates that  $\text{K}^+$  concentration adjacent to one  $\text{KTO}_{\text{pyr}}$  particle is in gradient descent guided by diffusion theory. As a comparison experiment, (K)PCN&KOH sample is synthesized by the substitution of KOH particles to  $\text{KTO}_{\text{pyr}}$  particles and presents a relatively homogeneous  $\text{K}^+$  distribution as shown in Fig. 2d. In detail, the atomic ratio of K/N is calculated at 3.7% approximately despite the fluctuation in the atomic level of N. Generally, KOH particles melt at  $360^\circ\text{C}$  concomitant with the crystalline structural destruction, and then free ions ( $\text{K}^+$  and  $\text{OH}^-$ ) spread smoothly and scatter randomly in PCN layers [34]. The distinction between these two  $\text{K}^+$  doping sources ( $\text{KTO}_{\text{pyr}}$  and KOH) can be interpreted substantially that  $\text{KTO}_{\text{pyr}}$  particles maintain the ion release capacity in the stable structure, leading to the steady continuous  $\text{K}^+$  point-diffusion and the consequent  $\text{K}^+$  radiate gradient distribution, while on the contrary the homogeneous doping is ascribed to the unconstrained mobility of isolated ions which release in quantity once KOH particles melt and vanish totally. To further verify the contribution of point-diffusion to gradient doping, we use another analogous  $\text{K}^+$  doping source: perovskite-type  $\text{KTaO}_3$  particles ( $\text{KTO}_{\text{per}}$ ) which possess much abundant  $\text{K}^+$  and also display a superior thermal structural stability. Interestingly,  $\text{K}^+$  doping is not observed in (K)PCN& $\text{KTO}_{\text{per}}$  sample (Figure 2bi) as the atomic ratio of K/Ta keeps constant at almost 1 (Table S1) and K/N is negligible (Fig. 2d). The difference roots in the relative repressed motion of  $\text{K}^+$  inside  $\text{KTO}_{\text{per}}$  particles because of its regular atomic arrangement and ordered crystal structure [26,45], in spite of the same elementary composition and constitutional unit as that of  $\text{KTO}_{\text{pyr}}$  particles.

For the further demonstration of gradient doping radiated from  $\text{KTO}_{\text{pyr}}$  particles, RISE is employed to vividly monitor the spatial  $\text{K}^+$  distribution with the doping effect on the PCN substrate. Based on the middle-angle BSE imaging, the gradient effect is investigated along the marked straight line with two clusters of  $\text{KTO}_{\text{pyr}}$  particles as endpoints.

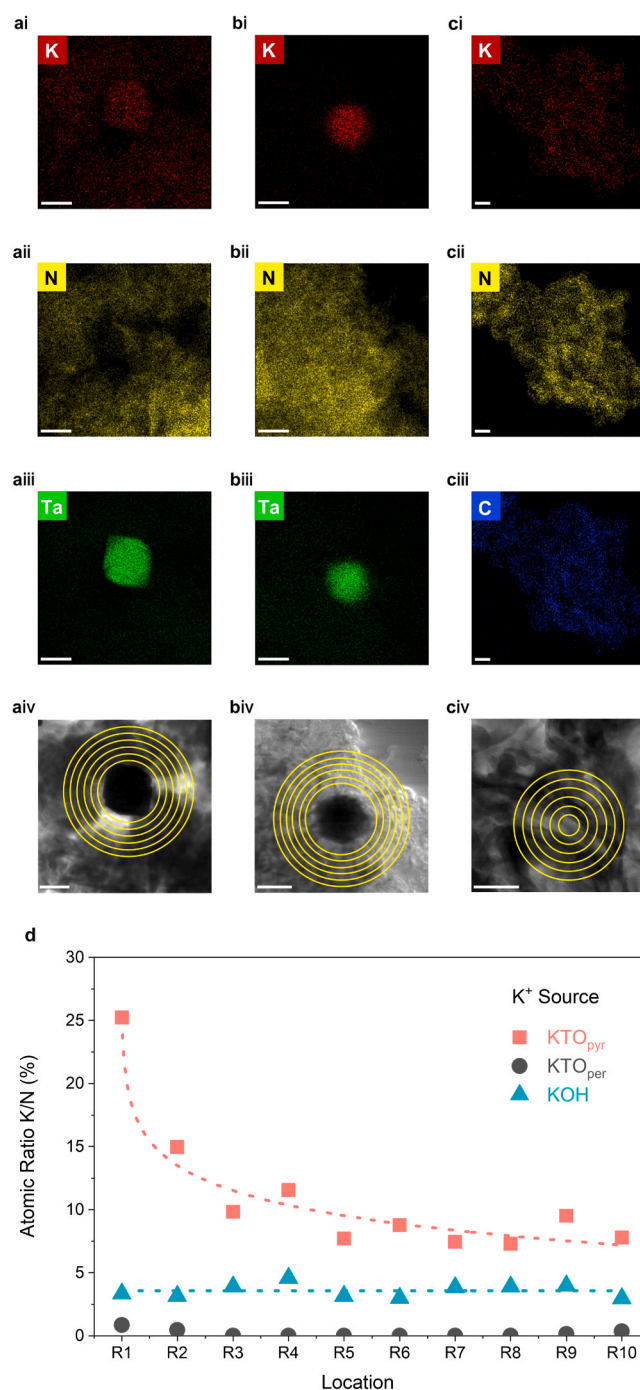


**Fig. 2.** ai-aiv for (K)PCN&KTO sample, bi-biv for (K)PCN& $\text{KTO}_{\text{per}}$  sample, ci-civ for (K)PCN&KOH sample. ai-ci and aii-cii are the corresponding EDS mapping of K and N respectively, whilst aiii-biii are representative of Ta with ciiv for C. aiv-civ, Bright field TEM images. All scale bars are 200 nm.

d, For the comparison of three  $\text{K}^+$  sources, the semiquantitative concentration distributions are displayed as atomic ratios of K/N collected from 10 concentric rings with corresponding radiuses in arithmetic sequence and for clarity 5 of them are displayed at intervals as marked yellow in aiv-civ. The average K/N within each ring (R1 to R10) is statistically analyzed from inside to outside and the source particles ( $\text{KTO}_{\text{pyr}}$  and  $\text{KTO}_{\text{per}}$ ) are enclosed by the innermost circle on purpose.

The specific Raman spectra successively collected at five equidistant points (Fig. 3a, b) are illustrated in Fig. 3c without subtracting the baseline. Regardless of the fluorescence interference caused by PCN, two sections of Raman shift peaks are nonetheless observed clearly for (K)

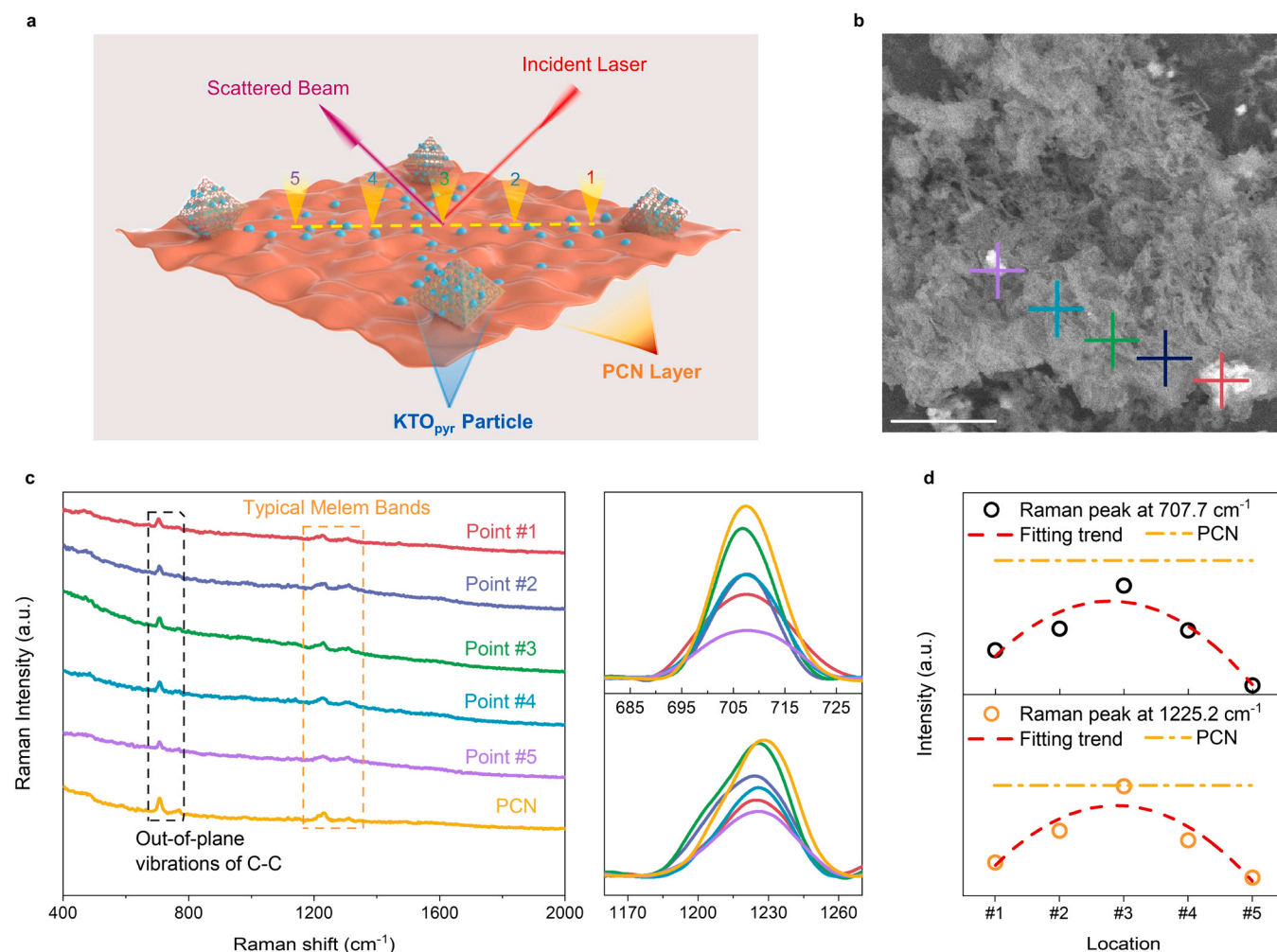


**Fig. 3.** a-b, The BSE image (b) with the scale bar of 1  $\mu\text{m}$  and five tagged collected points are schematized via RISE measurement (a), which is recorded on (K) PCN&KTO sample. c-d, Raman spectra (c) at five points (#1–5) compared to pristine PCN with corresponding magnified windows of two dotted sections after smoothing and the variation trend of Raman intensity with the location (d).

PCN&KTO sample. For pristine PCN, one section (in black dotted box) confined at around  $706\text{ cm}^{-1}$  is assigned to the in-plane rotation of sixfold rings in a graphitic carbon nitride layer as the typical signal for graphitic PCN, and the other section (in orange dotted box) ranging from  $1250\text{ cm}^{-1}$  to  $1350\text{ cm}^{-1}$  belongs to the disordered D bands for the melem structure [46,47]. The consistency in featured peaks among all five acquisition points suggests the structural similarity in basic frameworks. Compared to intrinsic signals of PCN (marked yellow), a declining trend in Raman intensity of both two peaks is presented for all points and in particular the signal from the middle point (marked green) is closest to pristine PCN as displayed in magnified windows. The electron redistribution induced by the interaction of  $\text{K}^+$  with active N atoms should be responsible for the diminishing intensity (in black dotted box) [36]. The weakening in peak intensity (in orange dotted box) is ascribed to the ring-opening in particle's vicinity where  $\text{K}^+$  is concentrated. As plotted by position (Fig. 3d), the approximately symmetrical ascending and then descending tendency reflects that  $\text{K}^+$  doping concentration indeed shows a downward trend with the distance from the doping source. Specifically, the doping effect is intensified in the position adjacent to the doping source, while it gradually weakens in the distant area and ultimately regresses to pristine PCN. Therefore, the contour of  $\text{K}^+$  concentration in PCN layers with the rugged terrain is conservatively realized.

The doping effects of  $\text{K}^+$  on PCN frameworks, with regard to structural and chemical properties, are unraveled by correlative spectral

characterizations from multi-perspective as discussed in **Supplementary 2.5** (Fig. S3-8, Table S1-4). It is worth noting that the unique saturated doping level is the compelling evidence sustaining the diffusion-controlled ion release and it is beneficial to avoid the overwhelming doping level which would result in structural deterioration and deep energetic impurity level (**Supplementary Part 2.6 and 2.7**).

Furthermore, to unveil the doping effect on band structure for particulate semiconductor samples, valence band (VB) XPS spectra are recorded with the assistance of Mott-Schottky (M-S) plots and Tauc plots. Conduction and valence band parameters are measured (Fig. S9, 10) and summarized in Table S5 (determination details are provided in **Supplementary Part 2.14**). It is found that for (K)PCN&KTO-x sequence, CBM presents a consecutive downward shift whereas valence band maximum (VBM) almost keeps consistent with the increasing doping level of  $\text{K}^+$ , as illustrated in (Fig. S11). The influence of doping concentration on the band gap and band position for  $\text{K}^+$  doped PCN is further investigated by DFT calculations as illustrated in Fig. 4. Independent discussions of  $\text{K}^+$  concentration and ring-opening respectively for the doping effect on band structures are considered inadvisable because the conversion of functional groups is inevitably accompanied with  $\text{K}^+$  embedding [33–35]. Hence, three model structure groups (A-C) with both two factors simultaneously taken into account are calculated and analyzed, and the corresponding optimized C-N configurations are displayed in Fig. S12. In group A with the suppose that each embedding  $\text{K}^+$  contributes to one adjacent ring open, band gap gradually narrows in

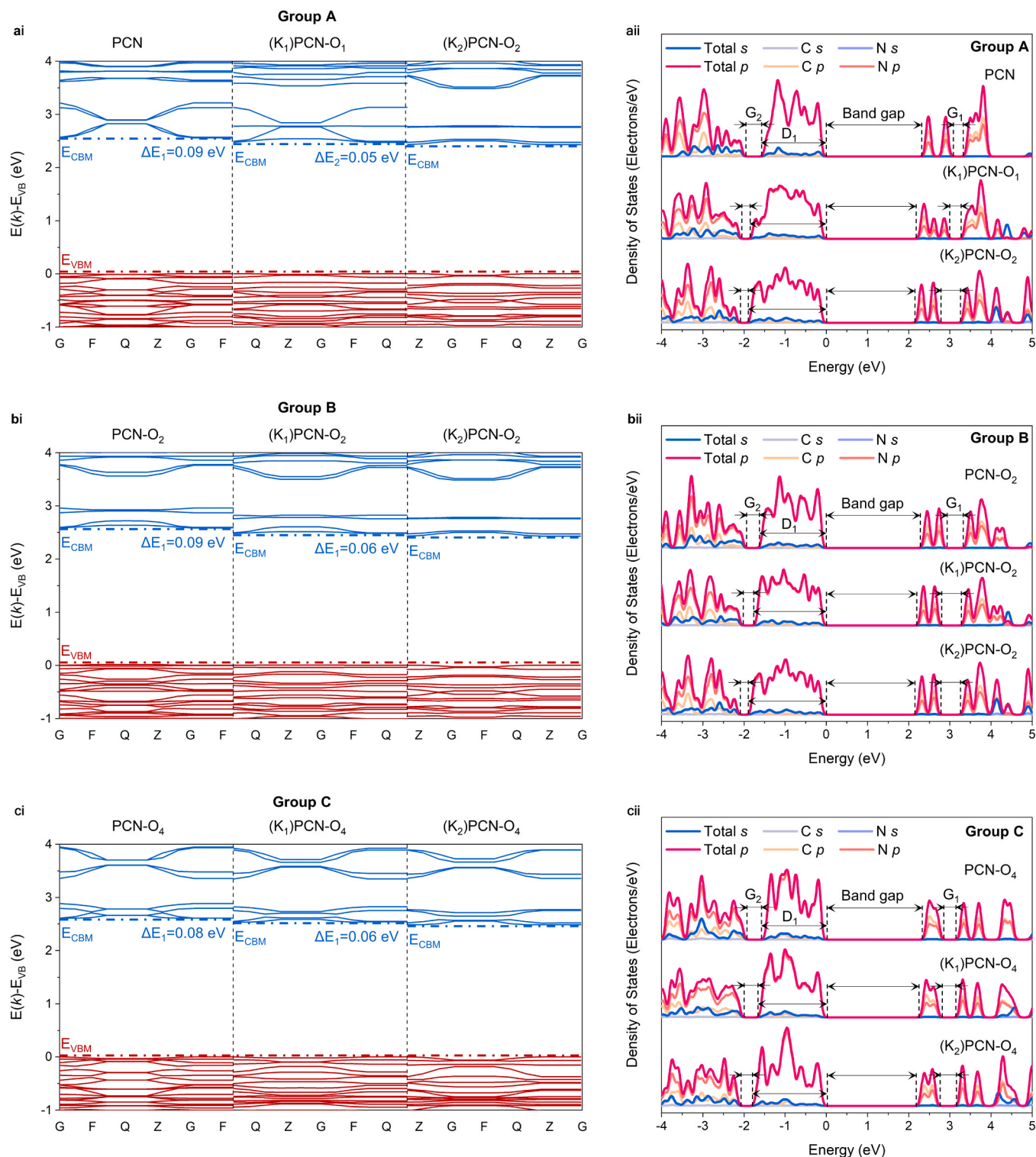


**Fig. 4.** ai-ci, calculated band structures. aii-cii, the density of states. ai-aii for the comparison of group A containing pristine PCN, (K<sub>1</sub>)PCN-O<sub>1</sub> and (K<sub>2</sub>)PCN-O<sub>2</sub> models, bi-bii for the comparison of group B containing PCN-O<sub>2</sub>, (K<sub>1</sub>)PCN-O<sub>2</sub> and (K<sub>2</sub>)PCN-O<sub>2</sub> models and ci-cii for the comparison of group C containing PCN-O<sub>4</sub>, (K<sub>1</sub>)PCN-O<sub>4</sub> and (K<sub>2</sub>)PCN-O<sub>4</sub> models.

sequence and CBM level displays a step-like drop from PCN to (K<sub>1</sub>)PCN-O<sub>1</sub> ( $\Delta E_1 = 0.09$  eV) and from (K<sub>1</sub>)PCN-O<sub>1</sub> to (K<sub>2</sub>)PCN-O<sub>2</sub> ( $\Delta E_2 = 0.05$  eV). Similar tendencies of band gap are concluded from group B with half of rings open and group C with all rings open. One point should be emphasized that although K<sup>+</sup> does not participate in the formation of band edge, it actually works on the band gap with band edge position [41,42]. Besides, it is worth mentioning that the VBM range (D<sub>1</sub>) and the

energy gap in CB (G<sub>1</sub>) broaden with K<sup>+</sup> embedding whereas the energy gap in VB (G<sub>2</sub>) shows an opposite trend, indicating the influence of K<sup>+</sup> and ring-opening on sp<sup>2</sup> orbital hybridization. The table s induced by vast nitrogen vacancy defects [34,48,49] is not found as it is circumvented by the saturated doping level, which is supported by the EPR and UV-vis DRS survey. Based on the experimental and simulation results, a consecutive downward shift in CBM along the upward concentration



gradient of  $K^+$  can be logically extrapolated as illustrated in the band bending schematic (Fig. S13). The inhomogeneous contour of  $K^+$  concentration results in the uneven potential contour of CBM with ups and downs (Fig. 1e) and consequently the superimposed built-in electric-field is enhanced by the reinforced horizontal anisotropy and impels photo-induced electrons to the peak where CBM potential is at a relative positive level, which is different from the typical one-dimensional band bending.

The consecutive band bending in CBM with the concomitant strengthened built-in electric-field acts a pivotal role in inhibiting the recombination probability and elevating the separation efficiency of photo-excited charge carriers. In comparison with pristine PCN and (K)PCN&KOH samples, the multilocal gradient doped (K)PCN&KTO sample exhibits a weaker emission intensity as shown in steady-state photoluminescence spectra (Fig. S14). Considering the stronger photon absorption of (K)PCN&KTO sample (Fig. S3), it could be concluded that less proportion of excited-state electrons should relax to the ground-state via photoluminescence [35]. The longer average lifetime ( $\tau_{avg}$ ) of carriers for (K)PCN&KTO sample (Fig. 5a) indicated the faster separation and lower recombination probability, as determined in Table S6. The carriers' average lifetime of (K)PCN&KOH is promoted by 40% compared to PCN, while the carriers' average lifetime of (K)PCN&KTO is prolonged by 60% compared to PCN. Thus, the promotion ability of average photo-induced carriers' lifetime is about three-fold compared to the traditional  $K^+$  doping PCN. Furthermore, the charge transfer resistance  $R_{ct}$  (reflected by the semicircle radius) of (K)PCN&KTO sample is found much lower compared with pristine PCN and (K)PCN&KOH sample (Fig. 5b), implying the boost in the directional migration of electrons. Besides, it is also confirmed by the lower slope in the M-S plot (Fig. S10b) for (K)PCN&KTO sample corresponding to better electron mobility according to the M-S equation.

The modulated reinforced charge transfer is therefore applied for elevating the photocatalytic and photoelectrochemical abilities in

hydrogen evolution from water splitting. About two-fold improvement in the performances of transient photocurrent response (Fig. 5c) and photocatalytic hydrogen evolution (Fig. 5d) compared to the optimal (K)PCN&KOH sample, can be attributed to the multilocal gradient  $K^+$  doping strategy with the engineered band bending structure. The substitution of amine groups by cyano groups arising from  $K^+$  doping is responsible for the photocatalytic improvement (eight-fold) compared to pristine PCN, as pendant amine groups have been proven as deep energetically trapping sites and adverse to the carriers migration [32, 35]. However, no activity enhancement for either (K)PCN&KTO<sub>per</sub> or (K)PCN&KTO(M) samples is ascribed to the absence of  $K^+$  doping (Fig. 5d). Because the saturated doping level of  $K^+$  avoids the introduction of defect energy level, photocatalytic and photoelectrochemical performances exhibit no significant deterioration with the excessive doping source addition (Fig. S15–17). It further demonstrates that a tuning consecutive downshift in CBM consequently accelerates photocatalytic hydrogen generation rate in agreement with the enhanced mobility of photoexcited electrons (Fig. 5a–c). The slight reduction during the consecutive photocatalytic test (Fig. 5f) assisted with the contrast of pre- and post-reaction indicates considerable photocatalytic stability (Fig. S18, 19). The apparent quantum yield (AQY) is then measured in function of the light wavelength, as shown in Fig. 5e. The AQY values at 400 nm and 420 nm are determined to be 21.8% and 10.4%, respectively (Table S7). Additionally, we have ruled out the possibility that the origination of the enhanced photocatalytic activity comes from the increased specific surface area (Table S8), KTO<sub>pyr</sub> (Fig. S20–22), cyano groups (Fig. S23). The contrast of variable  $K^+$  sources for comparison in terms of the photocatalytic activity under visible light irradiation is shown in Fig. S24. The photocatalytic activity for pure water splitting has also been discussed, as shown in Fig. S25, 26. As for  $K^+$  doping PCN, the multilocal  $K^+$  gradient-doping PCN shows the highest AQY compared with previous relevant doping researches, as shown in Table S9.

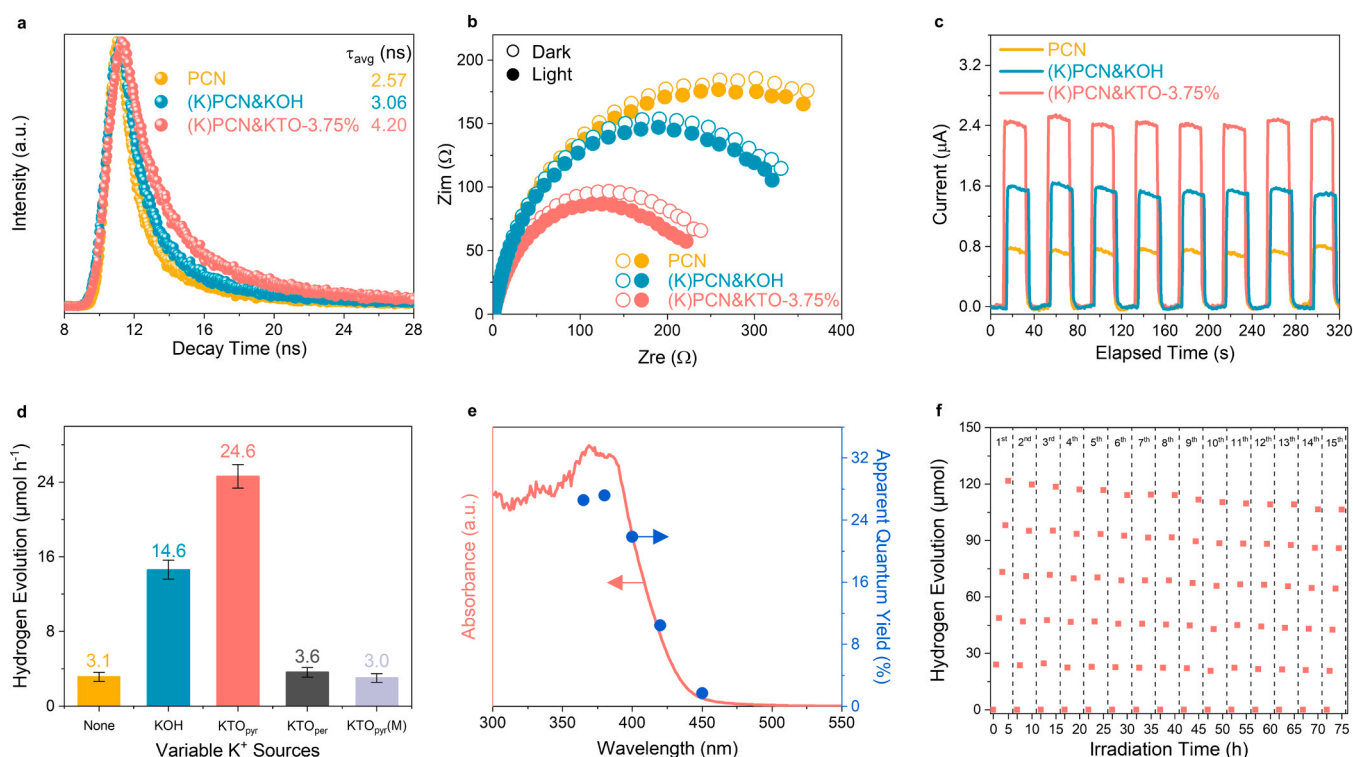


**Fig. 5.** a–c for the comparison of pristine PCN, (K)PCN&KOH and (K)PCN&KTO samples. a, Time-resolved transient photoluminescence (PL) decay spectra. b, Electrochemical and photoelectrochemical impedance spectroscopy (EIS and PEIS). c, Transient photocurrent response under visible light illumination. d, Activity contrasts of different  $K^+$  doping sources with regard to photocatalytic hydrogen evolution from water splitting. Error bars are noted with black line. e–f, The apparent quantum yield (e) and cycle stability tests (f) of photocatalytic hydrogen generation performance on (K)PCN&KTO sample.

Further studies were performed to provide additional evidence for the universality and controllability of this multilocal gradient-doping technique. The intercalation of A-site ion ( $K^+$  and  $Na^+$ ) in the pyrochlore structure is concluded from the reverse peak shift, as shown in Fig. S1a, in the substitution of  $Na^+$  for  $K^+$  and subsequently  $K^+$  for  $Na^+$ . So, pyrochlore-type  $Na_2Ta_2O_6$  (NTO) can be derived from  $KTO_{pyr}$  due to the ion exchange via thoroughly blending  $KTO_{pyr}$  particles in NaOH solution. (Na)PCN&NTO sample also exhibits a superior performance than (Na)PCN&NaOH sample, as shown in Fig. S29. As illustrated in Fig. S28, the  $K^+$  diffusion degree in PCN is strongly correlated with the reaction temperature and time. Compared with pristine PCN, 550–1 h and 550–2 h samples exhibit an over six-times improvement due to the multilocal gradient doping distribution in the certain diffusion time, while sample-4 h exhibits only three-times improvement as a result of the uniform distribution in the sufficient diffusion.

#### 4. Conclusion

On the whole, this work first contrives a multilocal gradient-doping technique implemented on particulate semiconductors via the controlled ion point-diffusion by applying ion storage materials as doping sources. Although this technique is realized in PCN in this work, it may be promoted to the other semiconductors with different kinds of ion-sustained release nano-capsules, which will show broad significance in photocatalysis and other photoelectric conversion fields.

#### CRedit authorship contribution statement

**Jiawei Yan:** Formal analysis, Writing of original draft; lead. **Wen-jian Fang:** Formal analysis, Writing of original draft; Lead. **Zhidong Wei:** Funding acquisition; Equal. **Jiasheng Chi:** Investigation; Equal. **Mingxia Chen:** Investigation; Equal. **Zhi Jiang:** Investigation; Supporting. **Kun Jiang:** Formal analysis; Supporting. **Shaohua Shen:** Project administration; Supporting. **Wenfeng Shangguan:** Funding acquisition, Formal analysis, Project administration; Lead.

#### Declaration of Competing Interest

The authors declare that they have no known competing financial interests or personal relationships that could have appeared to influence the work reported in this paper.

#### Data availability

Data will be made available on request.

#### Acknowledgements

This work was supported by the National Key Basic Research and Development Program (2018YFB1502001), the National Natural Science Foundation of China (No.21773153; No.22102095), the Basic science (Natural science) research project of higher education in Jiangsu Province (23KJB480011), the Centre of Hydrogen Science of Shanghai Jiao Tong University, China. We gratefully acknowledge the Instrumental Analysis Center of SJTU for structural characterizations. We also thank professor Kadi Zhu (School of Physics and Astronomy, SJTU) for the discussion about potential wells.

#### Appendix A. Supporting information

Supplementary data associated with this article can be found in the online version at [doi:10.1016/j.apcatb.2023.123155](https://doi.org/10.1016/j.apcatb.2023.123155).

#### References

- [1] J.H. Kim, D. Hansora, P. Sharma, J.-W. Jang, J.S. Lee, Toward practical solar hydrogen production - an artificial photosynthetic leaf-to-farm challenge, *Chem. Soc. Rev.* 48 (2019) 1908–1971.
- [2] T. Hisatomi, K. Domen, Reaction systems for solar hydrogen production via water splitting with particulate semiconductor photocatalysts, *Nat. Catal.* 2 (2019) 387–399.
- [3] Q. Wang, K. Domen, Particulate photocatalysts for light-driven water splitting: mechanisms, challenges, and design strategies, *Chem. Rev.* 120 (2020) 919–985.
- [4] S. Chen, T. Takata, K. Domen, Particulate photocatalysts for overall water splitting, *Nat. Rev. Mater.* 2 (2017) 1–17.
- [5] R. Chen, F. Fan, C. Li, Unraveling charge-separation mechanisms in photocatalyst particles by spatially resolved surface photovoltage techniques, *Angew. Chem. Int. Ed.* 61 (2022), e202117567.
- [6] R. Chen, F. Fan, T. Dittrich, C. Li, Imaging photogenerated charge carriers on surfaces and interfaces of photocatalysts with surface photovoltage microscopy, *Chem. Soc. Rev.* 47 (2018) 8238–8262.
- [7] D. Zhao, Y. Wang, C.-L. Dong, Y.-C. Huang, J. Chen, F. Xue, S. Shen, L. Guo, Boron-doped nitrogen-deficient carbon nitride-based Z-scheme heterostructures for photocatalytic overall water splitting, *Nat. Energy* 6 (2021) 388–397.
- [8] Q. Wang, T. Hisatomi, Q. Jia, H. Tokudome, M. Zhong, C. Wang, Z. Pan, T. Takata, M. Nakabayashi, N. Shibata, Y. Li, I.D. Sharp, A. Kudo, T. Yamada, K. Domen, Scalable water splitting on particulate photocatalyst sheets with a solar-to-hydrogen energy conversion efficiency exceeding 1, *Nat. Mater.* 15 (2016) 611–615.
- [9] T. Takata, J. Jiang, Y. Sakata, M. Nakabayashi, N. Shibata, V. Nandal, K. Seki, T. Hisatomi, K. Domen, Photocatalytic water splitting with a quantum efficiency of almost unity, *Nature* 581 (2020) 411–414.
- [10] R. Li, F. Zhang, D. Wang, J. Yang, M. Li, J. Zhu, X. Zhou, H. Han, C. Li, Spatial separation of photogenerated electrons and holes among {010} and {110} crystal facets of  $BiVO_4$ , *Nat. Commun.* 4 (2013) 1432.
- [11] J. Zhu, S. Pang, T. Dittrich, Y. Gao, W. Nie, J. Cui, R. Chen, H. An, F. Fan, C. Li, Visualizing the nano cocatalyst aligned electric fields on single photocatalyst particles, *Nano Lett.* 17 (2017) 6735–6741.
- [12] J. Narvaez, F. Vasquez-Sancho, G. Catalan, Enhanced flexoelectric-like response in oxide semiconductors, *Nature* 538 (2016) 219–221.
- [13] J.-P. Colinge, C.-W. Lee, A. Afzal, N.D. Akhavan, R. Yan, I. Ferain, P. Razavi, B. O'Neill, A. Blake, M. White, A.-M. Kelleher, B. McCarthy, R. Murphy, Nanowire transistors without junctions, *Nat. Nanotechnol.* 5 (2010) 225–229.
- [14] L. Jung, J. Pries, T.W. Maß, M. Lewin, D.S. Boyuk, A.T. Mohabir, M.A. Filler, M. Wuttig, T. Taubner, Quantification of Carrier Density Gradients along Axially Doped Silicon Nanowires Using Infrared Nanoscopy, *ACS Photonics* 6 (2019) 1744–1754.
- [15] L. An, M. Kitta, A. Iwase, A. Kudo, N. Ichikuni, H. Onishi, Photoexcited electrons driven by doping concentration gradient: flux-prepared  $NaTaO_3$  photocatalysts doped with strontium cations, *ACS Catal.* 8 (2018) 9334–9341.
- [16] H. Huang, B. Dai, W. Wang, C. Lu, J. Kou, Y. Ni, L. Wang, Z. Xu, Oriented built-in electric field introduced by surface gradient diffusion doping for enhanced photocatalytic  $H_2$  evolution in CdS nanorods, *Nano Lett.* 17 (2017) 3803–3808.
- [17] H.W. Qiao, S. Yang, Y. Wang, X. Chen, T.Y. Wen, L.J. Tang, Q. Cheng, Y. Hou, H. Zhao, H.G. Yang, A gradient heterostructure based on tolerance factor in high-performance perovskite solar cells with 0.84 Fill Factor, *Adv. Mater.* 31 (2019), e1804217.
- [18] W.S. Subhani, K. Wang, M. Du, X. Wang, S. Liu, Interface-modification-induced gradient energy band for highly efficient  $CsPbBr_2$  perovskite solar cells, *Adv. Energy Mater.* 9 (2019) 1803785.
- [19] H. Zhang, D. Li, W.J. Byun, X. Wang, T.J. Shin, H.Y. Jeong, H. Han, C. Li, J.S. Lee, Gradient tantalum-doped hematite homojunction photoanode improves both photocurrents and turn-on voltage for solar water splitting, *Nat. Commun.* 11 (2020) 4622.
- [20] F.A. Chowdhury, M.L. Trudeau, H. Guo, Z. Mi, A photochemical diode artificial photosynthesis system for unassisted high efficiency overall pure water splitting, *Nat. Commun.* 9 (2018) 1707.
- [21] Z. Luo, C. Li, S. Liu, T. Wang, J. Gong, Gradient doping of phosphorus in  $Fe_2O_3$  nanoarray photoanodes for enhanced charge separation, *Chem. Sci.* 8 (2017) 91–100.
- [22] F. Wang, W. Septina, A. Chemseddine, F.F. Abdi, D. Friedrich, P. Bogdanoff, R. van de Krol, S.D. Tilley, S.P. Berglund, Gradient Self-Doped  $CuBi_2O_4$  with Highly Improved Charge Separation Efficiency, *J. Am. Chem. Soc.* 139 (2017) 15094–15103.
- [23] Y. Fang, X. Li, Y. Wang, C. Giordano, X. Wang, Gradient sulfur doping along polymeric carbon nitride films as visible light photoanodes for the enhanced water oxidation, *Appl. Catal., B* 268 (2020), 118398.
- [24] Y. Xiao, C. Feng, J. Fu, F. Wang, C. Li, V.F. Kunzelmann, C.-M. Jiang, M. Nakabayashi, N. Shibata, I.D. Sharp, K. Domen, Y. Li, Band structure engineering and defect control of  $Ta_3N_5$  for efficient photoelectrochemical water oxidation, *Nat. Catal.* 3 (2020) 932–940.
- [25] T.A. Vanderah, I. Levin, M.W. Lufaso, An unexpected crystal-chemical principle for the pyrochlore structure, *Eur. J. Inorg. Chem.* 2005 (2005) 2895–2901.
- [26] S. Zlotnik, S.K. Sahu, A. Navrotsky, P.M. Vilarinho, Pyrochlore and perovskite potassium tantalate: enthalpies of formation and phase transformation, *Chem. Eur. J.* 21 (2015) 5231–5237.
- [27] Y. Zheng, L. Lin, B. Wang, X. Wang, Graphitic carbon nitride polymers toward sustainable photoredox catalysis, *Angew. Chem. Int. Ed.* 54 (2015) 12868–12884.

- [28] X. Zou, Y. Zhang, Noble metal-free hydrogen evolution catalysts for water splitting, *Chem. Soc. Rev.* 44 (2015) 5148–5180.
- [29] H. Gao, S. Yan, J. Wang, Y. an Huang, P. Wang, Z. Li, Z. Zou, Towards efficient solar hydrogen production by intercalated carbon nitride photocatalyst, *Phys. Chem. Chem. Phys.* 15 (2013) 18077–18084.
- [30] X. Wang, K. Maeda, A. Thomas, K. Takanabe, G. Xin, J.M. Carlsson, K. Domen, M. Antonietti, A metal-free polymeric photocatalyst for hydrogen production from water under visible light, *Nat. Mater.* 8 (2009) 76–80.
- [31] G. Zhou, Y. Shan, Y. Hu, X. Xu, L. Long, J. Zhang, J. Dai, J. Guo, J. Shen, S. Li, L. Liu, X. Wu, Half-metallic carbon nitride nanosheets with micro grid mode resonance structure for efficient photocatalytic hydrogen evolution, *Nat. Commun.* 9 (2018) 3366.
- [32] S. An, G. Zhang, K. Li, Z. Huang, X. Wang, Y. Guo, J. Hou, C. Song, X. Guo, Self-Supporting 3D Carbon Nitride with Tunable  $n \rightarrow \pi^*$  Electronic Transition for Enhanced Solar Hydrogen Production, *Adv. Mater.* (2021), e2104361.
- [33] V.W.-H. Lau, I. Moudrakovski, T. Botari, S. Weinberger, M.B. Mesch, V. Duppel, J. Senker, V. Blum, B.V. Lotsch, Rational design of carbon nitride photocatalysts by identification of cyanamide defects as catalytically relevant sites, *Nat. Commun.* 7 (2016) 12165.
- [34] H. Yu, R. Shi, Y. Zhao, T. Bian, Y. Zhao, C. Zhou, G. in Waterhouse, L.-Z. Wu, C.-H. Tung, T. Zhang, Alkali-assisted synthesis of nitrogen deficient graphitic carbon nitride with tunable band structures for efficient visible-light-driven hydrogen evolution, *Adv. Mater.* 29 (2017) 1605148.
- [35] Y. Zhao, P. Zhang, Z. Yang, L. Li, J. Gao, S. Chen, T. Xie, C. Diao, S. Xi, B. Xiao, C. Hu, W. Choi, Mechanistic analysis of multiple processes controlling solar-driven  $H_2O_2$  synthesis using engineered polymeric carbon nitride, *Nat. Commun.* 12 (2021) 3701.
- [36] W. Yan, L. Yan, C. Jing, Impact of doped metals on urea-derived g- $C_3N_4$  for photocatalytic degradation of antibiotics: Structure, photoactivity and degradation mechanisms, *Appl. Catal., B* 244 (2019) 475–485.
- [37] W. Fang, J. Liu, L. Yu, Z. Jiang, W. Shangguan, Novel (Na, O) co-doped g- $C_3N_4$  with simultaneously enhanced absorption and narrowed bandgap for highly efficient hydrogen evolution, *Appl. Catal., B* 209 (2017) 631–636.
- [38] Y. Hu, H. Gu, Z. Hu, W. Di, Y. Yuan, J. You, W. Cao, Y. Wang, H.L. Chan, Controllable Hydrothermal Synthesis of  $KTa_{1-x}Nb_xO_3$  Nanostructures with Various Morphologies and Their Growth Mechanisms, *Cryst. Growth Des.* 8 (2008) 832–837.
- [39] G.K.L. Goh, S.M. Haile, C.G. Levi, F.F. Lange, Hydrothermal synthesis of perovskite and pyrochlore powders of potassium tantalate, *J. Mater. Res.* 17 (2002) 3168–3176.
- [40] W. Guo, P. Yu, H. Luo, J. Chi, Z. Jiang, X. Liu, W. Wen, W. Shangguan, Unveiling the role of surface heterostructure in  $Bi_{0.5}Y_{0.5}VO_4$  solid solution for photocatalytic overall water splitting, *J. Catal.* 406 (2022) 193–205.
- [41] T. Xiong, W. Cen, Y. Zhang, F. Dong, Bridging the g- $C_3N_4$  interlayers for enhanced photocatalysis, *ACS Catal.* 6 (2016) 2462–2472.
- [42] G. Dong, K. Zhao, L. Zhang, Carbon self-doping induced high electronic conductivity and photoreactivity of g- $C_3N_4$ , *Chem. Commun.* 48 (2012) 6178–6180.
- [43] M. Matsunami, T. Hashizume, A. Saiki, Ion-exchange reaction of A-Site In  $A_2Ta_2O_6$  pyrochlore crystal structure, *Arch. Metall. Mater.* 60 (2015) 941–944.
- [44] Ismunandar, B.J. Kennedy, B.A. Hunter, Surface segregation and oxygen vacancy ordering in defect pyrochlores, *J. Solid State Chem.* 130 (1997) 81–89.
- [45] R. Perriot, B.P. Uberuaga, R.J. Zamora, D. Perez, A.F. Voter, Evidence for percolation diffusion of cations and reordering in disordered pyrochlore from accelerated molecular dynamics, *Nat. Commun.* 8 (2017) 618.
- [46] P. Niu, L.-C. Yin, Y.-Q. Yang, G. Liu, H.-M. Cheng, Increasing the visible light absorption of graphitic carbon nitride (melon) photocatalysts by homogeneous self-modification with nitrogen vacancies, *Adv. Mater.* 26 (2014) 8046–8052.
- [47] J. Xu, L. Zhang, R. Shi, Y. Zhu, Chemical exfoliation of graphitic carbon nitride for efficient heterogeneous photocatalysis, *J. Mater. Chem. A* 1 (2013) 14766.
- [48] X. Zhang, P. Ma, C. Wang, L. Gan, X. Chen, P. Zhang, Y. Wang, H. Li, L. Wang, X. Zhou, K. Zheng, Unraveling the dual defect sites in graphite carbon nitride for ultra-high photocatalytic  $H_2O_2$  evolution, *Energy Environ. Sci.* 15 (2022) 830–842.
- [49] X. Wang, J. Meng, X. Zhang, Y. Liu, M. Ren, Y. Yang, Y. Guo, Controllable approach to carbon-deficient and oxygen-doped graphitic carbon nitride: robust photocatalyst against recalcitrant organic pollutants and the mechanism insight, *Adv. Funct. Mater.* 31 (2021) 2010763.